

Sparse Representation of Targets with Mixed Scattering Primitives

John Lee, Peter J. Collins, and Julie Ann Jackson

Department of Electrical and Computer Engineering
Air Force Institute of Technology, Dayton, OH 45433 USA
John.Lee.Ctr@afit.edu, Peter.Collins@afit.edu, Julie.Jackson@afit.edu

Abstract — A combination of two scattering primitives – wedge diffraction primitives and isotropic point scatterers – is used to reconstruct far-field monostatic scattering patterns of several target geometries and addresses shortcomings of traditional approaches that only use a single type of primitive (e.g., approximations in analytic solutions, slow convergence). An l_1 -norm minimization technique is applied to determine a set of weights for the point scatterers. We show that combining these two types of primitives yields better reconstruction performance than when each primitive type is used individually.

Index Terms — Geometric Theory of Diffraction (GTD), l_1 -norm minimization, Radar Cross Section (RCS), scattering primitives, sparse representation, Uniform Theory of Diffraction (UTD).

I. INTRODUCTION

It is well known that far-field scattering from a complex geometry can be estimated by decomposing the target into simple scattering primitives and summing their individual responses. Reconstruction of electromagnetic field quantities with isotropic point scatterers (IPSs) is a fundamental principle in SAR and ISAR processing [1]. The use of non-isotropic scattering primitives has also been investigated in [2,3]. Moreover, in [4], a dense array of IPSs is used as a part of an overcomplete dictionary. Sparse representations enable discrimination of target returns from nuisance returns that can arise from the measurement process.

In this work, we also seek to reduce the number of scattering centers required by introducing a wedge diffraction primitive (WDP) derived from GTD/UTD theory. We use the WDP to capture known scattering mechanisms based on the target's far-field pattern and allow the IPSs to recover the remaining coherent differences. We limit the analysis of this approach to planar cuts of 2D geometries and compare the results to reference data generated by a 3D Method of Moments (MoM) code. A normalization factor is applied to translate 2D echo width predictions to 3D RCS.

The use of multiple primitive types is also considered under the context of compressive sensing (CS). The theory states that the number of measurements required to successfully recover the sparse representation of a far-field pattern (via Basis Pursuit or other l_1 -norm minimization algorithms) decreases substantially (even below the Nyquist sampling rate) as signal sparsity increases [5]. We posit that the sparsity of the far-field pattern representation can be improved by using WDPs to capture diffraction behavior and IPSs to capture the remaining difference between the diffraction contributions and the original far-field pattern. For example, a large portion of the monostatic response from a 2D flat plate can be accurately represented with two WDPs located at the ends of the plate. In contrast, a solution with two IPSs can only capture the specular response and would require significantly more points to accurately reconstruct the sidelobes of the monostatic return.

While sparsity can be satisfied, the efficacy of this technique as an application for CS is also dependent on the bounds of the Restricted Isometry Property (RIP) of the measurement matrix [6]. Determining these bounds explicitly is an NP-hard problem, but numerical experiments can provide a cursory and empirical assessment of its performance.

In the following sections, we describe the theory behind reconstruction via scattering centers and describe the framework that was developed to perform the reconstruction with a mixed set of primitives. We then present two simple cases to validate our approach, discuss the implications of their results and describe additional areas of investigation.

II. SCATTERING CENTER THEORY

Consider a collection of spatially distributed scattering centers, each associated with a complex coefficient that modulates its magnitude and phase [7]. By adjusting the location and the complex value of each scattering center, the superposition of every scattering center's far-field response may yield a pattern that matches the far-field response of an arbitrary target

geometry. This concept is illustrated in Fig. 1 (a) and concisely summarized as:

$$S_{IPS}^{pred}(k, \hat{\mathbf{r}}) = \sum_{n=1}^N \gamma_n e^{-j2k\hat{\mathbf{r}} \cdot \mathbf{r}'_n}, \quad (1)$$

where S_{IPS}^{pred} is the far-field value synthesized with the wavenumber k and observed from direction $\hat{\mathbf{r}}$. S_{IPS}^{pred} is determined by the summation of N IPSs that are located at \mathbf{r}'_n and modulated by the complex coefficient γ_n . The components of γ_n control the magnitude and phase delay applied to the IPSs, while the operating frequency and the locations of the scattering centers with respect to the phase origin affect the exponential term in (1) and alters the phase oscillation rate of the far-field pattern.

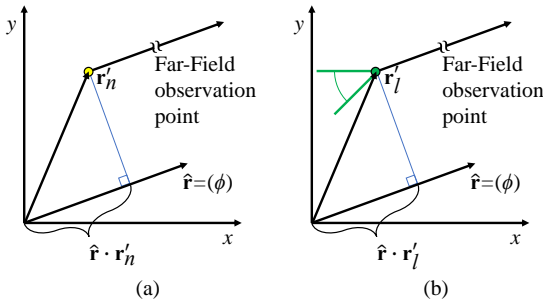


Fig. 1. Far-Field approximation of a (a) IPS and (b) WDP.

WDPs, shown in Fig. 1 (b), are coherently summed together in a similar fashion as IPSs to generate far-field patterns. From [8], UTD diffraction coefficients reduce to GTD coefficients when the surfaces of the wedge are flat and the observation angles are not in the transition regions near the shadow boundaries. We implement 2D WDPs as:

$$D^{s,h}(\phi, m) = \frac{-e^{j\pi/4} \sin(\pi/m)}{2m\sqrt{2\pi k}} \left[\left(\frac{1}{\cos \frac{\pi}{m}} \right) \mp \left(\frac{1}{\cos \frac{\pi}{m} - \cos \frac{2\phi}{m}} \right) \right], \quad (2)$$

where $m = (2\pi - \alpha)/\pi$, α is the wedge angle and ϕ is the monostatic observation angle. In the second term between the brackets, the negative term corresponds to the soft polarization, while the positive term corresponds to the hard polarization (in our case, θ and ϕ polarization, respectively). This 2D analytic solution assumes that the diffraction edge is always aligned along the z -axis and extends towards infinity. The RCS of a finite wedge of width w can be determined by multiplying the 2D echo width by $2\pi w^2/\lambda$, where wavelength $\lambda = 2\pi/k$. The diffraction coefficient $D^{s,h}$ replaces the IPS coefficient γ_n in (1) and yields:

$$S_{WDS}^{pred}(k, \hat{\mathbf{r}}) = \sum_{l=1}^L D_l^{s,h} e^{-j2k\hat{\mathbf{r}} \cdot \mathbf{r}'_l}, \quad (3)$$

to generate the far-field monostatic backscatter of the L diffracting wedges.

We note that the formulation in (2) is valid for wedge angles of up to 180° and does not address dihedral effects. Moreover, the scattering pattern arising from WDPs exhibit asymptotic behavior for monostatic angles that are normal to the faces of the wedge due to their vicinity to the shadow boundaries. These singularities occur in pairs for finite length wedges and additional considerations need to be made when geometries contain dihedral or concave regions.

III. OPTIMIZATION FRAMEWORK

We use the IPS and WDP formulations to estimate a solution S_{FF}^{est} for S_{FF}^{ref} by considering,

$$\begin{aligned} S_{FF}^{ref} &\approx S_{FF}^{est} = S_{WDS}^{pred} + \Delta p \\ &= S_{WDS}^{pred} + (S_{FF}^{ref} - S_{WDS}^{pred}) \\ &= S_{WDS}^{pred} + S_{IPS}^{pred}, \end{aligned} \quad (4)$$

where S_{WDS}^{pred} utilizes a priori information about the geometry to generate a coarse estimate of S_{FF}^{ref} and the coherent difference Δp is estimated with S_{IPS}^{pred} . An optimization framework, depicted in Fig. 2, was designed to determine S_{WDS}^{pred} in a preprocessing stage and S_{IPS}^{pred} with a sparse optimization stage.

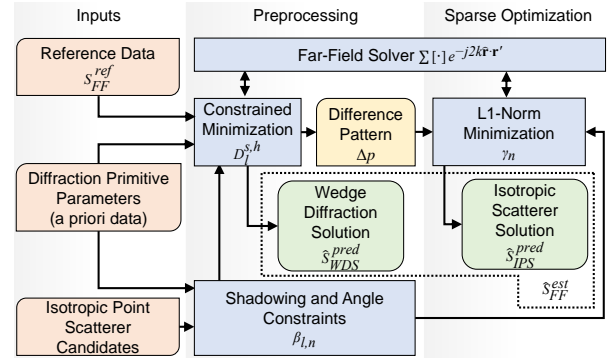


Fig. 2. Optimization framework.

The framework was generalized to use a constrained minimization routine to estimate appropriate parameter values for multiple types of non-isotropic scattering primitives (including the WDP utilized in this study). We note that the determination of \mathbf{r}'_l and the dependent variables of $D_i^{s,h}$ in (3) can be a non-trivial problem with many local minima, especially when a priori information is limited. Because our investigation is focused on the feasibility of reducing the number of IPSs, we bypass the constrained minimization in these experiments and provide parameter values for the WDPs based on a priori knowledge of the scattering geometry as inputs instead.

The preprocessing stage synthesizes a far-field pattern from the WDPs and applies a global phase shift to the prediction that best matches the reference data. This is a necessary step in the event that the reference

data and WDP prediction from the analytic geometry have different phase origins. The phase-shifted WDP solution is then coherently subtracted from the S_{FF}^{ref} to yield Δp .

Shadowed regions are also determined in the preprocessing stage of the framework to prevent WDPs and IPSs from radiating through the boundaries of the target geometry. This is performed by tracing a vector from each primitive and scattering center to all far-field observation points and determining whether the ray intersects a facet of the geometry [11].

Modifications to support shadowing and the phase shift of the WDP solution augment the model in (4) with additional modulation terms such that,

$$\begin{aligned} \hat{S}_{FF}^{est}(k, \hat{\mathbf{r}}) &= \hat{S}_{WDS}^{pred} + \hat{S}_{IPS}^{pred} \\ \hat{S}_{FF}^{est}(k, \hat{\mathbf{r}}) &= \sum_{l=1}^L \beta_l e^{j\psi} S_{WDS}^{pred} + \sum_{n=1}^N \beta_n S_{IPS}^{pred} \\ &= \sum_{l=1}^L \beta_l D_l^{s,h} e^{-j(2k\hat{\mathbf{r}} \cdot \mathbf{r}'_l - \psi)} + \sum_{n=1}^N \beta_n \gamma_n e^{-j2k\hat{\mathbf{r}} \cdot \mathbf{r}'_n}, \end{aligned} \quad (5)$$

where $\beta_{l,n}$ represent the shadowing and angle constraints applied to the WDSs and IPSs respectively and $e^{j\psi}$ represents the phase shift applied to the WDP solution.

In the sparse optimization stage, determining appropriate values of \mathbf{r}'_n and γ_n in (1) often relies on l_1 -norm minimization techniques such as Basis Pursuit DeNoising (BPDN) in [4]. We note that BPDN provides a solution that minimizes the sum of the magnitudes of the complex coefficients, whereas an l_0 -norm minimized solution minimizes number of complex coefficients contributing to the solution (true sparsity). A solution arising from an l_1 -norm minimization routine is a good approximation to the l_0 -norm minimized solution when compressive sensing characteristics are met, namely that the basis set that is used to represent the signal satisfies the RIP. Again, determining adherence to the RIP can be computationally intractable for non-random matrices, therefore we proceed to apply this technique with the understanding that l_1 -norm minimized solutions may not strictly be the sparsest solution. In our framework, the SPGL1 library was leveraged to perform the BPDN optimization [9].

We note that primitive-based approaches are popular because generating far-field scattering from the primitives is straightforward. This is a key benefit and allows the optimization routine to iterate more quickly than in alternative approaches [10].

IV. NUMERICAL EXPERIMENTS

We first apply our framework on a single flat plate, to demonstrate that the WDPs are implemented correctly and that BPDN can recover an adequate solution to Δp . Next, the framework is applied to an angled plate, which includes a dihedral response that cannot be captured with

the WDPs and shall be recovered with the IPSs. Figure 3 illustrates the two test geometries that are used to validate our approach.

The flat plate geometry is a 1m x 0.1m plate with zero thickness, while the angled plate geometry consists of a 1m x 0.125m and a 0.5m x 0.125m plate joined at one end to form a 90° angle (the latter dimension of each geometry is used to translate 2D echo width to 3D RCS). While the flat plate has no thickness, two variations of the angled plate were generated: one with zero thickness and one with 0.01m thickness. The significance of the angled plate variations is discussed in Section IV-B.

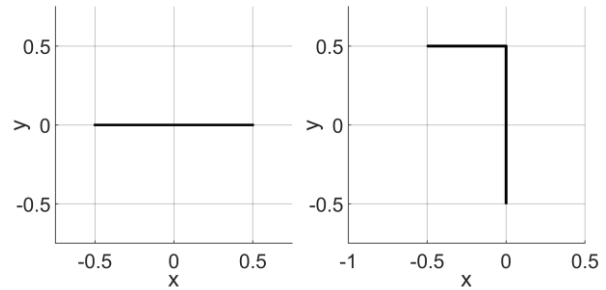


Fig. 3. Flat plate and angled plate test geometries.

For all cases, only the points on the $z=0$ plane were used since the far-field patterns were limited to the xy -plane (elevation $\theta=90^\circ$, azimuth $\phi=[0, 360^\circ]$) and there is no variation in either geometry in the z -direction. In all cases, we calculated the TM-polarized far-field backscatter response at 6 GHz ($\lambda=0.05\text{m}$), ensuring that both targets are electrically large and amenable to high frequency approximations. Several mesh discretizations were generated to assess sparsity requirements for a given BPDN solution. Lastly, the BPDN parameters for error tolerance and maximum iterations were set to 10^{-3} and 10^3 , respectively, and were held constant over all experiments.

The reference data S_{FF}^{ref} in our comparisons was generated with a MoM-based code to mitigate any contribution from measurement artifacts. We utilize a relative error norm as our metric for comparison, calculated as $\sum_{k, \hat{\mathbf{r}}} \|S_{FF}^{ref} - \hat{S}_{FF}^{est}\|_2 / \|S_{FF}^{ref}\|_2$, where $\|\cdot\|_2$ is the l_2 -norm.

A. Flat plate

Figure 4 illustrates our results from the flat plate geometry and compares the reference data against our method: the top plot compares the reference data S_{FF}^{ref} against the diffraction solution from the preprocessing stage \hat{S}_{WDS}^{pred} as well as the combined solution $\hat{S}_{FF}^{est} = \hat{S}_{WDS}^{pred} + \hat{S}_{IPS}^{pred}$; the middle plot illustrates the performance of the sparse optimization stage by

comparing the IPS solution \hat{S}_{IPS}^{pred} with the difference pattern Δp that the optimization attempts to recover; finally, the bottom plot depicts the coherent difference between S_{FF}^{ref} and \hat{S}_{FF}^{est} .

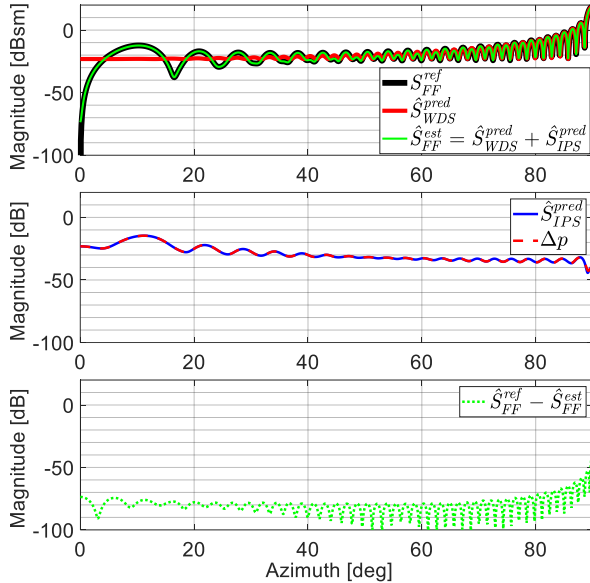


Fig. 4. Reference, WDP and IPS solutions for a flat plate (magnitude). Discrepancies between the reference and WDP solution (top) are corrected with an IPS solution (middle) to yield low reconstruction error (bottom).

\hat{S}_{WDS}^{pred} was generated by defining two WDPs at the ends of the plate with $\alpha=0^\circ$. The singularities from each primitive sum to generate the specular lobe at $\phi=90^\circ$. We observe that the diffraction solution compares well with the reference data until the monostatic angle approaches the grazing angle of the flat plate (a known deficiency in GTD analytic solutions). The coherent difference from the preprocessing stage stays largely within the -20 and -40 dB range and yields a relative error of 0.0731.

After \hat{S}_{WDS}^{pred} is generated, Δp is supplied to BPDN to synthesize \hat{S}_{IPS}^{pred} . The result of the sparse optimization stage shows a well-converged solution and has a coherent difference that is largely below -60 dB. When the WDP and IPS solutions are combined to yield \hat{S}_{FF}^{est} , we see overlay agreement with S_{FF}^{ref} . The combined solution achieves a relative error of 0.0011.

In contrast to our combined method, traditional scattering center reconstruction of far-field data utilizes IPSs exclusively to reconstruct the reference data rather than the delta pattern. We can assess the efficacy of the traditional approach by calculating the relative error as a function of the number of IPSs used to perform the reconstruction, as shown in Fig. 5. Using a $\lambda/3$ sampling

to generate the IPSs candidates provides $N=61$ points. We see that both methods require all points to achieve the lowest errors, and the traditional method achieves a relative error of 0.0019, compared to 0.0011 when the combined method is used (the WDP solution does not vary as a function of the number of IPSs).

We also observe that when scattering centers with the smallest magnitudes are removed from contributing to the far-field pattern, the error of the traditional approach increases more quickly than the combined approach. In this example, the traditional approach exceeds the error of the WDP solution when fewer than $N=60$ points are used for the reconstruction.

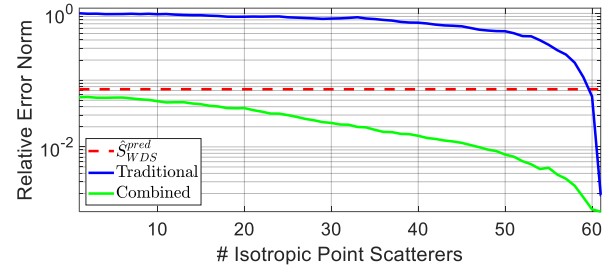


Fig. 5. Relative error norm of the flat plate.

These results indicate that a solution generated from a combination of WDPs and IPSs can achieve a more accurate reconstruction than either of the two separately. Moreover, for any desired level of error, the combined solution is sparser than the traditional method.

B. Angled plate

The angled plate geometry provides a more challenging far-field pattern to reconstruct than the flat plate. In addition to the flat plate responses, a strong dihedral response will occur in the far-field azimuth sector $\phi=(180^\circ, 270^\circ)$. Knowing that the current implementation of WDPs cannot reconstruct the dihedral response, we limit their contributions to angles exclusive of the dihedral sector via β_i in (5).

We note that even with the applied angle constraints, the WDPs may be inaccurate outside of the dihedral region, as well. According to [12], UTD WDPs fail near the shadow boundaries on concave shapes due to the fact that one of the WDPs is shadowed by obstructing geometry. The authors propose a separate type of diffraction coefficient to address dihedral effects by tracking rays that have multiple diffraction and reflection interactions on the target. Without introducing a third type of scattering center into the framework, we apply two additional WDPs located on the shared edge of the two plates (both with $\alpha=0^\circ$). This is analogous to two independent flat plates, where the additional WDPs complement the primitives on the open edges of the angled plate and compensate for the singularities that

arise from those primitives. In total, five WDPs are used: two for each flat plate and one for exterior corner of the angled plate and with $\alpha=90^\circ$. This arrangement yields a good approximation when compared to the reference data. The relative error norm over the far-field sector where the WDP solution is valid was calculated to be 0.0992 and is similar to the relative error norm achieved by the WDP solution for the flat plate geometry.

We note that IPSs will also encounter issues in pattern reconstruction of the angled plate due to the dihedral sector. We observed that the IPSs on a zero-thickness angled plate failed to generate an adequate reconstruction since there is a large contrast in the far-field response of the dihedral and non-dihedral regions. Implementing a finite thickness model, shown in Fig. 6, and enforcing shadow boundaries mitigated these effects: an optimization of the zero thickness geometry resulted in an error of 0.7210, while the finite thickness geometry achieved an error of 0.0477.

However, even with the finite thickness geometry, additional non-physical aberrations are evident in the solution. We can observe the source of these errors by considering the angle sectors where each IPS contributes to the far-field. These sectors are discretized and plotted as vectors in Fig. 6.



Fig. 6. Active IPSs for $\phi=[0^\circ, 270^\circ]$ (red vectors) and $\phi=[270^\circ, 360^\circ]$ (green vectors).

The figure indicates that there are IPSs located in the interior region of the angled plate that contribute to both the dihedral and non-dihedral sectors of the far-field response. Moreover, the number of interior points contributing to the non-dihedral sector varies as the shadow boundary sweeps across the interior sector of the angled plate from $\phi=[116^\circ, 180^\circ]$ and $[270^\circ, 296^\circ]$. This variation causes the discontinuities in the far-field pattern shown in Fig. 7 and we see that the severity of the discontinuities decrease when the rate of variation decreases, namely when angle approaches either of the normal incident angles ($\phi=180^\circ$ and 270°).

If the IPSs from the finite thickness model are used in the proposed method to reconstruct Δp for the entire azimuth range $\phi=[0^\circ, 360^\circ]$, these discontinuities significantly degrade the reconstruction in the regions where the \hat{S}_{WDS}^{pred} is already very good: under this arrangement, the method achieves a relative error norm of 0.0964 (0.0905 for $\lambda/4$, 0.0830 for $\lambda/5$). While it is

a slight improvement over the solution generated by WDPs alone, it does not provide a better solution than the traditional method. We speculate that, in addition to the discontinuities, the dynamic range of the delta pattern increases because the WDPs are restricted from contributing to the dihedral sector of S_{FF}^{ref} . These effects ultimately make Δp more difficult to reconstruct with IPSs.

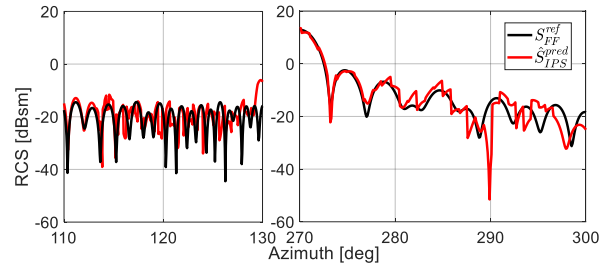


Fig. 7. Discontinuities in non-dihedral sector of IPS solution due to interior IPS contributions.

As an alternative, we enforce additional constraints on the finite thickness model via β_n such that the interior and exterior IPSs only contribute to the non-dihedral and dihedral sectors, respectively. Using this strict separation, \hat{S}_{FF}^{est} from the combined method yields an improved relative error norm of 0.0238 and exceeds the performance of the traditional method. The results of this experiment are shown in Fig. 8.

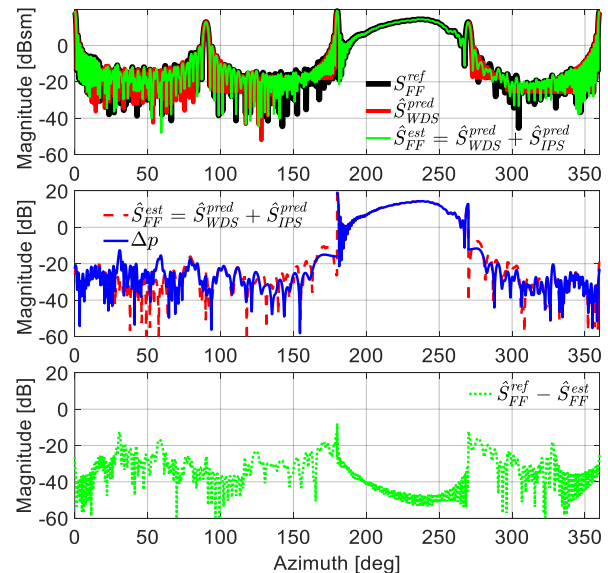


Fig. 8. Reference, WDP and IPS solutions for an angled plate (magnitude only). Discrepancies between the reference data and WDP solution (top) are corrected with an IPS solution (middle) to yield low reconstruction error (bottom).

The figure also clearly shows the large dynamic range of Δp where much of the dihedral sector stays above 0 dB and non-dihedral sector stays largely below -20 dB. With our proposed method of synthesizing \hat{S}_{FF}^{est} , the errors achieved mostly fall below -20 dB.

Mirroring the analysis performed on the flat plate, we assess the trade between relative error norm and the number of IPSs used in the reconstruction of S_{FF}^{ref} and Δp , shown in Fig. 9. We note that the figure includes an additional dataset to show that, while the strict separation of the contributions of the inner IPSs to the dihedral sector and the outer IPSs to the non-dihedral sector was an effective strategy for synthesizing Δp , it was not effective when the IPSs were used to reconstruct S_{FF}^{ref} . We speculate that the configuration that enforces strict separation does not provide an adequate number of IPSs to generate the narrow lobes that are present near the edges of the dihedral region in the far-field reference pattern. Conversely, the more permissive shadowing scheme provides enough of these point scatterers to generate narrow (but discontinuous) peaks to match the far-field reference pattern well, but detrimentally impacts the solution when they are used to match Δp (which has lower and wider lobes).

We also observe a discontinuity in the solutions that rely exclusively on IPSs whereas the flat plate tests exhibited a monotonically decreasing error. This is because the magnitudes of the coefficients supporting the dihedral sector are significantly higher than those supporting the non-dihedral sector. For example, in the test case where Δp was recovered via IPSs only, the removal of the lowest magnitude coefficients from reconstruction will incrementally degrade the non-dihedral sector and only after the 39th largest coefficient is removed will the dihedral reconstruction degrade.

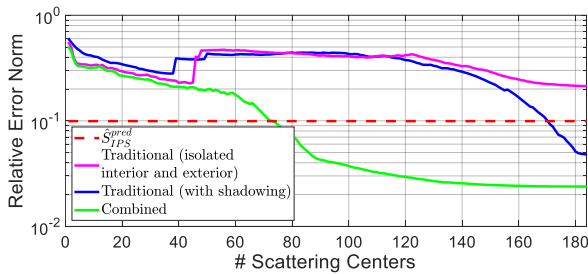


Fig. 9. Relative error norm of the angled plate.

Overall, the results are consistent with those in the flat plate experiment. That is, the traditional approach that utilizes only IPSs to reconstruct far-field reference data is unable to reach the error levels that are achieved with the proposed approach. Moreover, if the smallest (in magnitude) non-zero coefficients are discarded from the reconstruction, the degradation of the solution from the

proposed method is more gradual than the traditional method.

Our numerical experiments are summarized in Table 1. We see with both geometries that a lower error is achieved when combining a WDP solution with an IPS solution to the delta pattern instead of the relying exclusively on WDPs or IPSs to reconstruct the far-field data. In the case of the angled plate, the result required manually setting boundaries on the range of angles where each primitive type contributes to the far-field pattern. Nonetheless, this is a valuable insight—if the primary goal is to find a compact representation of far-field data, this approach would prove to be very useful. With the proposed method, we can achieve a lower error with approximately the same number of point scatterers (WDPs and IPSs). Likewise, we have solutions that degrade more slowly with respect to how many IPSs are used to reconstruct the pattern when the IPSs are applied to a delta pattern rather than the far-field data.

Table 1: Relative error and (total point scatterer count) of $\lambda/3$ discretized geometries

	Flat Plate	Angled Plate*
WDS Only	0.0731 (2)	0.0992 (5)
IPS Only	0.0019 (61)	0.0477 (184)
Combined	0.0011 (63)	0.0238 (189)

* WDS case evaluated for non-dihedral sector only.

V. SPARSE RECONSTRUCTION CONSIDERATIONS FOR COMPRESSIVE SENSING

In addition to investigating the reconstruction accuracy of the proposed method, we seek to understand how well IPSs perform as a sparse basis in the context of CS. With both the flat plate and angled plate geometries, we tested for solution convergence and robustness.

Figure 10 depicts the results from multiple discretizations of the flat plate geometry and how their solutions degrade as the weakest scattering centers are incrementally removed from the solution.

CS literature states that the recovery of signal is robust to noise and reconstruction accuracy should degrade gracefully with a given basis set due to the RIP (more specifically, the Null Space Property) [13]. We can see that the IPS basis can be used to reconstruct Δp in the proposed method and reconstruct S_{FF}^{ref} in the standard method. We noted previously that the degradation of \hat{S}_{FF}^{est} in the proposed method is more gradual than the far-field reconstruction in the standard method and we see that this remains true for other discretizations as well. However, the data also indicates that the solutions generated by the BPDN are not optimally sparse. The delta pattern and far-field pattern do not vary with respect to discretization, yet the number of IPSs required

to reconstruct those patterns does vary with respect to discretization.

We also observe that the numbers of candidate IPSs are $N=61, 81$ and 101 for $\lambda/3, \lambda/4$ and $\lambda/5$, respectively. At 6 GHz, the plate is 20λ long and the solutions are effectively using all of the available scattering centers to determine a solution, even though it is known that a sparser solution exists (because the coarse discretizations are able to recover an equally accurate solution with fewer IPSs). While BPDN determines solutions with the smallest $\sum_n |\gamma_n|$, it does not guarantee a solution that minimizes the cardinality of γ unless other CS criteria are met. These findings suggest that a basis set from IPSs does not satisfy the RIP.

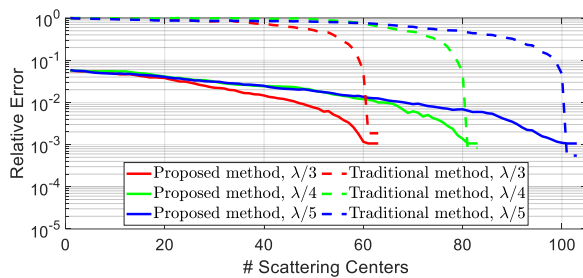


Fig. 10. Robustness of proposed and traditional method solutions for $\lambda/3$ to $\lambda/5$ discretizations of the flat plate.

A similar analysis is performed on the data for the angled plate dihedral region, depicted in Fig. 11. Again, the number of IPSs required to reach a given level of error depends on the number of available IPSs. The rate of degradation is different from the flat plate case, however: the presence of longer tails on the reconstructions with the proposed method suggest that they have converged and while they are not ideal and optimally sparse solutions, they seem to be sparser and more robust than the reconstructions with the traditional method.

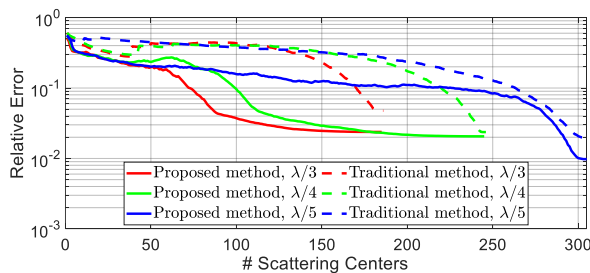


Fig. 11. Robustness of proposed and traditional method solutions for $\lambda/3$ to $\lambda/5$ discretizations of the angled plate.

These numerical experiments show that, while the technique is successful in generating point scatterer based (WDP and IPS) representations of the targets,

there may be limited utility as a basis for compressive sensing applications. The results show empirically that when a sparse representation of the target is used to generate far-field patterns (the traditional approach), perturbations in the sparse representation will introduce excessively large errors for the purpose of interpolation and extrapolation. The sparsity is slightly improved when IPS are employed to reconstruct delta patterns (the proposed approach), but their efficacy seems to be geometry dependent.

These initial results reveal areas that merit additional investigation. It would be prudent to integrate solutions for dihedral scattering mechanisms [14] into the framework which would allow the IPSs to recover a more simplified delta pattern. Additionally, we observed that the number of shadowed IPSs can vary rapidly and would introduce unwanted discontinuities in synthesized solution. Tapering or adjusting the angles that an IPS contributes to may address this issue and would improve how the IPSs perform on concave targets. Lastly, the optimization framework can be expanded to support multiple frequencies, multiple polarizations, non-planar observation geometries and bistatic quantities to possibly aid the convergence of the optimization routines and expand its applicability to a wider variety of test cases.

VII. CONCLUSION

Using WDPs in conjunction with IPSs to reconstruct far-field patterns shows merit in simple cases and when they are applied judiciously. In our numerical experiments, we show that this approach can reduce the overall number of scattering centers required to replicate the scattering response of a flat and a right-angled plate. We also observed that l_1 -norm minimization techniques may have difficulty finding maximally sparse solutions when IPSs are used as a basis set. Despite this, synthesized solutions are more robust when they are used to reconstruct a coherent difference pattern rather than the far-field data.

ACKNOWLEDGMENT

The views expressed in this paper are those of the authors, and do not reflect the official policy or position of the United States Air Force, Department of Defense, or the U.S. Government.

REFERENCES

- [1] M. A. Richards, J. A. Scheer and W. A. Holm, *Principles of Modern Radar: Basic Principles*. SciTech Publishing, Edison, NJ, 2010.
- [2] J. A. Jackson, "Parametric models for signature prediction and feature extraction," invited paper, *Applied Computational Electromagnetics Society (ACES) Journal*, vol. 34, no. 2, pp. 258-260, 2019.
- [3] J. Halman and R. J. Burkholder, "Sparse

- expansions using physical and polynomial basis functions for compressed sensing of frequency domain EM scattering,” *IEEE Antennas Wirel. Propag. Lett.*, vol. 14, pp. 1048-1051, 2015.
- [4] B. Fischer, I. Lahaie, M. Hawks, and T. Conn, “On the use of basis pursuit and a forward operator dictionary to separate specific background types from target RCS data,” *AMTA 36th Annual Meeting and Symposium*, pp. 85-90, 2014.
- [5] S. Foucart and H. Rauhut, *A Mathematical Introduction to Compressive Sensing*. Springer, New York, 2013.
- [6] E. J. Candes, J. Romberg, and T. Tao, “Robust uncertainty principles: Exact signal frequency information,” *IEEE Trans. Inf. Theory*, vol. 52, no. 2, pp. 489-509, 2006.
- [7] R. Bhalla, H. Ling, J. Moore, D. J. Andersh, S. W. Lee and J. Hughes, “3D scattering center representation of complex targets using the shooting and bouncing ray technique: a review,” *IEEE Antennas and Propagation Magazine*, vol. 40, no. 5, pp. 30-39, Oct. 1998.
- [8] D. A. McNamara, C. W. I. Pistorius, and J. A. G. Malherbe, *Introduction to The Uniform Geometrical Theory of Diffraction*. Artech House, Boston, MA, 1990.
- [9] E. van den Berg and M. P. Friedlander, “Probing the Pareto frontier for basis pursuit solutions,” *SIAM J. on Scientific Computing*, vol. 31, no.2, pp. 890-912, November 2008.
- [10] I. J. Lahaie, S. M. Cossmann, M. A. Blischke, V. Way, and A. Arbor, “A model-based technique with ℓ_1 minimization for defect detection and RCS interpolation from limited data,” *Applied Computational Electromagnetics Society (ACES) Journal*, vol. 28, no. 12, pp. 1171-1179, 2013.
- [11] J. Tuszynski, “Triangle/ray intersection,” *Mathworks File Exchange*. <https://www.mathworks.com/matlabcentral/fileexchange/33073-triangle-ray-intersection>
- [12] T. Griesser and C. A. Balanis, “Dihedral corner reflector backscatter using higher order reflections and diffractions,” *IEEE Trans. Antennas Propag.*, vol. 35, no. 11, pp. 1235-1247, 1987.
- [13] Y. C. Eldar and G. Kutyniok, *Compressed Sensing: Theory and Applications*. Cambridge University Press, NY, 2012.
- [14] J. A. Jackson, “Analytic physical optics solution for bistatic, 3D scattering from a dihedral corner reflector,” *IEEE Trans. Antennas Propag.*, vol. 60, no. 3, pp. 1486-1495, Mar. 2012.



John Lee Received his B.S. in Electrical and Computer Systems Engineering from Rensselaer Polytechnic Institute in 2005 and his M.S. in Electrophysics from New York University Tandon School of Engineering in 2012. He is currently pursuing his Ph.D. in Electrical Engineering at the Air Force Institute of Technology. He has previously worked for The Boeing Company in Southern California and is currently a Member of the Research Staff at Riverside Research in New York, NY. His current research interests are focused on electromagnetic applications of compressive sensing, RCS modeling, analysis and optimization.



Peter J. Collins is a Professor of Electrical Engineering with the Air Force Institute of Technology, Department of Electrical and Computer Engineering, Wright-Patterson AFB, OH. Collins’ research interests are in the areas of low observables, electromagnetic materials design, and remote sensing along with the underlying foundational disciplines of electromagnetic theory, computational electromagnetics, and signature metrology.

Collins is a Fellow of the Antenna Measurement Techniques Association (AMTA), Senior Member of the Institute of Electrical and Electronic Engineers (IEEE), and is author or co-author of over 90 technical papers, 2 book chapters, and 1 US Patent.



Julie Ann Jackson is an Associate Professor of Electrical Engineering at the Air Force Institute of Technology (AFIT), where she joined the faculty in 2009. She earned the B.S.E.E. degree from Wright State University, Dayton, OH, in 2002 and the M.S. and Ph.D. degrees from The Ohio State University, Columbus, OH, in 2004 and 2009, respectively. Her graduate studies were funded with fellowships from the National Science Foundation, the Dayton Area Graduate Studies Institute, The Ohio State University, and the Ohio Board of Regents. Jackson has held internships at the Air Force Research Laboratory, Alphatech, Inc., Jacobs Sverdrup, and Bell Laboratories. She is a Senior Member of the

IEEE, member of Eta Kappa Nu and Tau Beta Pi, and Chief Advisor for the Ohio Eta Chapter of Tau Beta Pi. Jackson was elected in 2018 to the IEEE AES Society Radar Systems Panel and serves on the technical program committees of the IEEE Radar Conference and the MSS Tri-Service Radar Conference. Jackson's contributions have been recognized with multiple awards including the 2019 IEEE Fred Nathanson

Memorial Radar Award, the Air University Civilian Quarterly Award in 2018, the Southwestern Ohio Council for Higher Education (SOCHE) 2016 Faculty Excellence Award, and the 2012 Air Force Science, Technology, Engineering, and Mathematics Award for Outstanding Scientist/Engineer, Junior Civilian. Her research interests are in radar signal processing and imaging and exploitation of RF signals.